PERGAMON

International Journal of Multiphase Flow 27 (2001) 817–842

International Journal of Multiphase Flow

www.elsevier.com/locate/ijmulflow

Three-dimensional measurements of single bubble dynamics in a small diameter pipe using stereoscopic particle image velocimetry

Yassin A. Hassan *, Javier Ortiz-Villafuerte, William D. Schmidl

Department of Nuclear Engineering, Texas A&M University, College Station, TX 77843-3133, USA

Received 13 September 1999; received in revised form 6 September 2000

Abstract

The particle tracking velocimetry combined with the shadow image measurement techniques were used to study the velocity field generated by the passage of a single air bubble through a small volume, as it was rising in quiescent water, in a small diameter pipe. This technique provides the velocity field in conjunction with the bubble size and shape. The tracer particles were first tracked through four consecutive frames, using a Hough transform and an architecture resonance theory 2 (ART 2) neural network. Then, the three-dimensional reconstruction of the flow field in the whole measurement volume was achieved through a stereoscopic matching technique. Detailed information about the three-dimensional reconstruction of the bubble shape, calibration, particle tracking, and stereoscopic vector matching algorithms is presented. Error analysis to evaluate the accuracy of the measurements is also included.

The effect of the wall on the flow field was studied by dividing the test volume into two regions; namely, center region and wall region. This allowed grouping similar bubble rise trajectories to perform conditional averages of the transient behavior of the velocity field. The vorticity generated from the velocity field is described and discussed for the bubble trajectory along the pipe core.

Keywords: Bubble dynamics; Bubble wake; Pseudo-turbulence; Stereoscopic PIV; Vorticity

1. Introduction

Bubbly flows play a key role in a variety of natural and industrial processes. For many years, the design of systems with bubbly flows was based primarily on empiricism (or empirical data). An

* Corresponding author. Tel.: +1-97984-57090; fax: +1-97984-56443.
E-mail address: y-hassan@tamu.edu (Y.A. Hassan).

0301-9322/01/$ - see front matter
PII: S0301-9322(00)00054-9

accurate and complete description of the phase interactions in two-phase bubbly flows is not available at this time. These phase interactions are, in general, three-dimensional and unsteady. Therefore, measurement techniques utilized to obtain qualitative and quantitative data from two-phase flows need to be extended to acquire transient and three-dimensional data. These techniques can provide information to test theoretical models and numerical simulations. For example, some of the new versions of thermal-hydraulic computer codes used in nuclear reactor safety analysis (such as RELAP and CATHARE programs) have new three-dimensional capabilities; however experimental data is still needed to validate the closure models implemented in these codes.

Local mass, momentum and energy transfer processes strongly depend on the magnitude of the local turbulence. In a turbulent two-phase bubbly flow, the total liquid turbulence is composed of the single-phase component, plus the random agitation generated by the bubble motion, which includes vortex shedding and wakes. Lance and Bataille (1991) denoted the bubble-generated turbulence as "pseudo-turbulence". In their experiments at low void fractions, it is determined that the isotropy of the liquid turbulent flow is preserved after injection of bubbles. In a two-phase bubbly flow, the surrounding flow disturbances generated by individual bubbles play an important role in the modeling of turbulence closure relationships needed in the time-averaged momentum equation. However, the local liquid turbulence, and the bubble/bubble and/or bubble/wake interactions also affect the bubble motion, which leads to a continuous feedback mechanism for turbulence enhancement and suppression. The understanding of such physical phenomena will have far-reaching benefits in upgrading the operation and efficiency of current modeling processes, and in supporting the development of new and innovative approaches for two-phase flow simulations.

All bluff bodies, including bubbles, generate near and far wakes as they rise. The bubble near wake is directly related to vortex formation at the bubble surface, vortex growth and vortex shedding (Fan and Tsuchiya, 1990). It is not possible to predict the precise instantaneous motion of a rising bubble without considering the dynamics of the wake. The experimentally observed zigzag or spiral path of ellipsoidal bubbles is associated with its wake structure. For example, Saffman (1956) explained the zigzag motion of an oblate bubble as due to the interaction of an oscillating wake and the instability motion near the front of the bubble. Whether the bubble follows a zigzag or spiral flow path depends on the physical properties of the liquid phase, and the way it is generated. Another phenomenon closely related to the wake dynamics is bubble orientation, measured as the attack angle. Fan and Tsuchiya (1990) refer to the wake as the region of non-zero vorticity through which the bubble has passed, in an otherwise uniform flow. The vortex aspect changes with respect to the relative velocity between the observer and the center of the vortex, as well as the vortex strength. Vortex structures may also be traveling at different relative velocities. Vorticity is considered an important quantity that needs to be determined for the understanding and description of turbulent flows. In two-phase turbulent flows, information about the vorticity field will improve the knowledge of structure of the flow.

Traditional single point flow measurement techniques provide simultaneous information of the flow at a limited number of locations, so the spatial resolution of the vorticity field is very poor. On the other hand, imaging techniques can describe both qualitatively and quantitatively the whole flow field, although the temporal resolution is usually low. Brücker (1999) used the particle image velocimetry technique to study the structure and dynamics of the wake behind bubbles following zigzag and spiral trajectories. It is concluded that the wake structure behind zigzagging

bubbles is a hairpin-like vortex. For a spiraling bubble, the wake consists of two streamwise vortex filaments attached to the bubble's rear. Lunde and Perkins (1997) found similar results during a flow visualization study.

Most of the work performed in single bubble dynamic studies do not consider the wall influence on bubble motion and shape. In many practical applications bubbles rise in narrow spaces, where the solid structure influence cannot be ignored. These applications include the steam generators, pressurizers, and fuel bundles of the nuclear power plants. Studies of the wall effect on rising bubbles generally deal with measurements of the decrease of the rise velocity and steady-state drag coefficient magnitudes (Tasuge and Hibino, 1975; Clift et al., 1978; Krishna et al., 1999). Uno and Kintner (1956) observed that the wall effect is negligible only if the ratio of the pipe diameter to the bubble equivalent diameter is at least 10. Maneri and Mendelson (1968) presented predictions of the rise velocity in bounded liquids based on wave theory. The influence of the wall on vortex shedding was experimentally studied by Bosch et al. (1996), who made their measurements on flow past square cylinders. These researchers found that there is a minimum gap width below which vortex shedding is completely suppressed. Hassan et al. (1998) obtained transient, 3D measurements of the flow field generated by a single air bubble rising in stagnant water in a small diameter pipe.

The objective of this experimental study is to demonstrate the capabilities of the stereoscopic particle tracking velocimetry technique to yield transient, 3D, full-volume information of the flow field for the two phases in a bubbly flow. Here, we present the velocity distribution of the flow field around a small air bubble rising in a stagnant liquid, in a small diameter pipe. The transient ensemble-averaged velocity fields are estimated. The bubble-pipe wall interaction and its influence on the liquid velocity field are studied. The vorticity field generated by the passage of the bubble is also described. A transient analysis of the kinetic energy in the test volume is also presented.

2. Experimental set-up and bubble reconstruction

A schematic of the experimental set-up and the camera configuration is shown in Fig. 1. Air bubbles of average size about 3-mm spherical-equivalent diameter were injected into a 12.7-mm i.d., 15.9-mm o.d., 1.3-m long Plexiglas tube filled with deionized water. The flow was seeded with 40-μm polystyrene tracer particles of density 1050 kg/m^3. The measurements were carried out at a location of about $L/D = 66$, where L is the length from pipe inlet to measurement zone, and D is the pipe inner diameter. In general, bubble terminal velocity is reached just a few bubble diameters after bubble release. Once the bubble reached the viewing volume it would have gained a velocity equal to the terminal velocity, if the wall influence was not present. The test section was enclosed in a rectangular Plexiglas box filled with water, with the same refractive index as that of the pipe. This was done to reduce the pipe optical curvature effect. In addition, as explained later, refraction effects were included in the calibration parameters. Four CCD cameras were utilized in this experimental investigation. The cameras were run in field mode with resolution of 640×240 pixels at 60 frame/s. A more detailed description of the experimental set-up is given by Hassan et al. (1999).

As shown in Fig. 1(b), one of the cameras is only used for bubble shape analysis. A shadow particle image velocimetry technique was developed to obtain accurate data of size, shape,

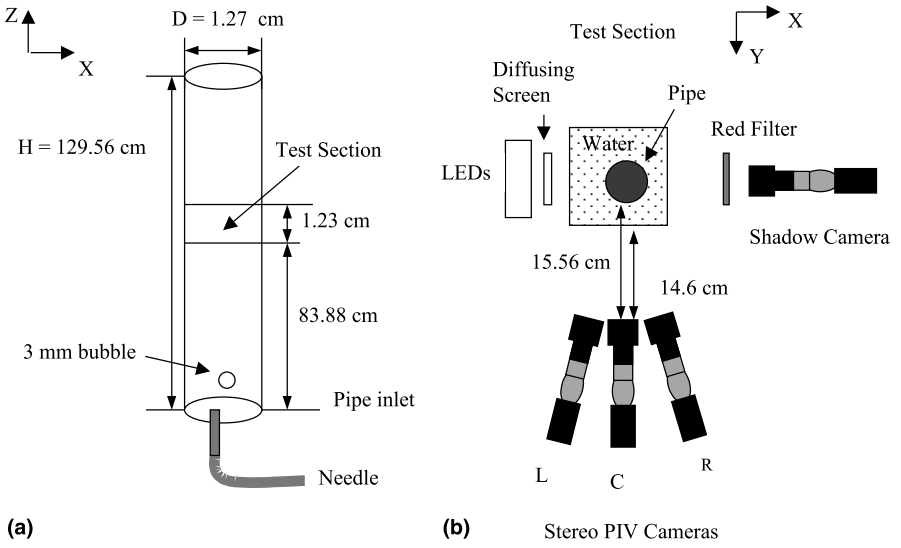

Fig. 1. Facility setup and camera configuration.

trajectory, and orientation of the bubble. This technique allowed capturing the image of the shadow of the bubble by employing forward scattering. Light emitting diode (LED) units emitting red light coupled with a diffusing screen were used to illuminate the test volume. A red filter was placed in front of the shadow camera to detect the red light images only. Once the images of the bubble are acquired with both PIV and shadow cameras, the direct generalized Hough transform (DGHT) algorithm (Leavers, 1992; Ortiz-Villafuerte, 1999) was employed to compute the centroid, rotation angle, and semiaxes of the ellipse that best fits the edge points of the bubble image. This algorithm was only applied to images from the orthogonally-positioned PIV center camera C (PIVC) and shadow camera S (PIVS), as illustrated in Fig. 1(b).

Fig. 2 shows typical images acquired by the PIVS and the PIVC cameras. Fig. 3 shows the origin of coordinates and the notation for the parameters that define the reconstructed bubble. The origin of coordinates was located at the base and center of the cylindrical test volume. The four cameras were positioned such that the z coordinate had similar alignment for all cameras. Consequently, all the cameras had the same coordinate value of the bubble centroid z_b and the semiaxis length c. In addition, the image planes of the PIVC camera and the PIVS camera were parallel to the XZ and YZ world planes, respectively. Thus, the bubble images from the PIVS camera yielded information to compute the bubble centroid coordinates y_b and z_b, the semiaxes lengths b and c; and, β, the angle between the Z-axis and semiaxis b. The PIVC camera bubble images yielded information to compute the coordinate x_b, the semiaxis length a and, α, the angle between the Z-axis and semiaxis a. As an example, using the bubble images in Fig. 2, it was determined that this bubble was located at $x_b = -0.16$, $y_b = -1.99$, and $z_b = 3.86$ mm. The values of the semiaxes were: $a = 1.24$; $b = 1.46$; and $c = 1.39$ mm. The rotation angles about the Y- and X-axes were $\alpha = -4°$, and $\beta = 25°$, respectively.

The scale factors were 38.8, 39.7, and 39.3 pixel/mm on the X-, Y-, and Z-directions, respectively. The 3D reconstruction process was applied to 57 pairs of bubble images. The statistical analysis yielded the following average values of the semiaxes: $a = 1.25$, $b = 1.45$, and $c = 1.36$

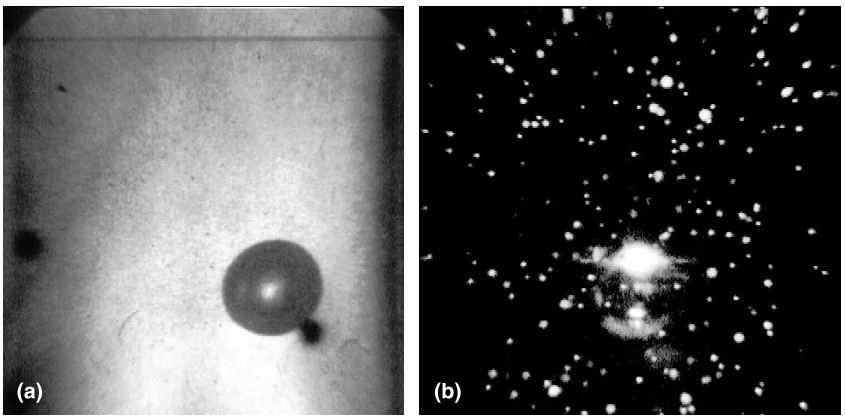

Fig. 2. Typical images acquired by the shadow (a) and center PIV (b) cameras when the bubble is present in the test volume. These two images allow for the three-dimensional reconstruction of the bubble shape.

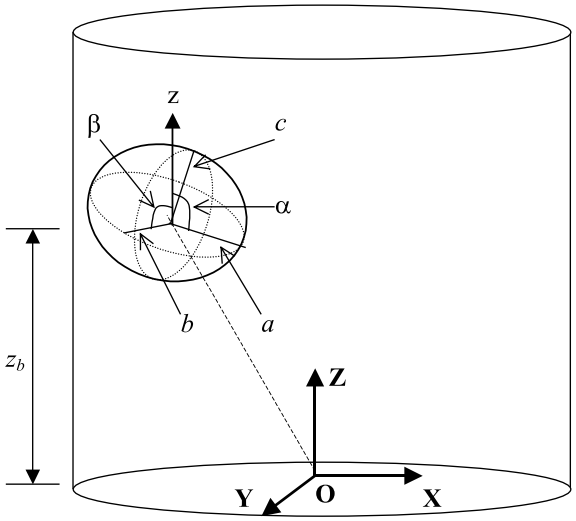

Fig. 3. Coordinates of the test volume and notation for bubble parameters, where a is the semiaxis in the X-direction; b the semiaxis in the Y-direction; c the semiaxis in the Z-direction; α the angle between the Z-direction and a; and β is the angle between the Z-direction and b.

mm, with standard deviations of 0.10, 0.08, and 0.08 mm, respectively. Thus, the bubble can be considered to have a shape close to an oblate spheroid. The maximum error on the dimensions and centroid location found in the reconstruction process was always less than 3 pixel (0.08 mm). The complete error analysis is given by Ortiz-Villafuerte (1999).

3. Camera calibration

Camera calibration is the technique from which camera parameters are determined using a set of image points with known world coordinates. Such parameters include camera position in the

world coordinate system and orientation. Also, internal camera parameters, such as focal length, or principal point distance, lens distortion parameters, etc. can be computed through camera calibration. Although perspective projection is non-linear, a series of linear transformations can relate a point P of world coordinates (x, y, z) to an image point I of coordinates (u, v), if projective coordinates are used. The linear transformations consist of translation and rotation of the projective center of the camera as a rigid body, followed by a perspective transformation (Gonzalez and Wintz, 1987; O'Hern et al., 1997). The perspective projection equations are given by:

$$u = \frac{t_{11}x + t_{12}y + t_{13}z + t_{14}}{t_{31}x + t_{32}y + t_{33}z + 1}, \tag{1}$$

$$v = \frac{t_{21}x + t_{22}y + t_{23}z + t_{24}}{t_{31}x + t_{32}y + t_{33}z + 1}, \tag{2}$$

where it was assumed that P is not on the focal plane of the camera, and t_{34} was set to 1 to uniquely specify the so-called perspective matrix **T**. Eqs. (1) and (2) have combined 11 unknowns, so at least six non-coplanar image-point coordinates and their corresponding world-point coordinates are needed to solve for the 11 t_{ij}'s. These equations are similar to the derived ones by Abdel-Aziz and Karara (1971), which is known as the direct linear transformation (DLT) method.

In order to include all refraction effects in the calibration parameters of the DLT method, the image and world coordinates of the calibration points must be obtained in the same conditions in which the measurements are carried out. This alternative presents the problem of constructing a test, or calibration setup, which must be placed exactly on the same position where the actual experimental set-up would be located. This is achieved by utilizing accurately spaced points on a grid. The grid is mounted on a high precision micrometer, which can be displaced on the X-, Y-, and Z-directions. In our case, 546 points were used for the calibration, and the Eqs. (1) and (2) were solved by using a least squares method for each camera. Once the unknown parameters are determined, we have a relationship between world and image points for each camera. To uniquely determine the three world coordinates of an image point we need at least two images of that point from cameras at different view angles. By using the image coordinates of a point from the two cameras, and the already known t_{ij}'s for each camera, a system of four equations (Eqs. (1) and (2) for each camera) can be solved for the unknown x, y, and z, by using a least squares technique.

4. Data processing and 3D stereoscopic reconstruction

The recorded images are directly digitized via framegrabbers. Prior to employing the tracking routines, an initial processing stage is employed. The gray scales and the particle center of gravity are estimated. Then a 2D tracking (in u, v coordinates) of the seed particle images is used. The tracking routine algorithms employed in this study were developed by Hassan and Philip (1997). Recently, numerous schemes have been developed to achieve the matching of the seed images among the frames. Examples of these routines are auto and cross-correlations, depending on double images on the same frame, or single image on a single frame, respectively. Tracking routines among multiple frames include neural networks and genetic algorithms. In this study, a neural network is used. The tracking process starts by selecting a seed particle image in the first

frame, and locating all the particle images in the next three frames, that fall in the search region of the first particle, as can be seen in Fig. 4. In order to find out which of the particles in four consecutive frames had proper alignment, the Hough transform (Hough, 1962; Leavers, 1993) was utilized. The Hough transform mapped the u and v coordinates of the particle image into angle (measured from u-axis) and intercept (with the v-axis) data. Those particles existing on a line were clustered in a tight region in the Hough space. This can be easily seen by considering a couple of image points (u_1, v_1) in frame 1 and (u_2, v_2) in frame 2, as illustrated in Fig. 4. These two points define a unique straight line, whose equation can be written as $v = m_0 u + b_0$. If another seed–particle–image point (u_3, v_3) in frame 3 is considered, two other values of m and b can be computed, namely m_1, b_1, and m_2, b_2. If those are equal to m_0 and b_0, respectively, this new image point (u_3, v_3) lies on the same straight line as (u_1, v_1) and (u_2, v_2); otherwise new lines are defined. Thus, in the mb plane (or parameter space) each new pair (m,b) will determine the same point exactly, if the image point of a seed particle (u_i, v_i) is on the same line as (u_1, v_1) and (u_2, v_2). Digitization effects and camera resolution adversely affect the calculation of image centroids so (m_i, b_i) will not be exactly the same for image points lying on the same line. Since the flow is disturbed, the seed particles do not necessarily follow a straight path. However, the particle paths are approximately linear from frame to frame for short time intervals. A problem can occur when computing the slope m when its value is infinite. Thus, we used the angle θ between the u-axis and the line determined by (u_i, v_i) and (u_j, v_j) as the parameter for the description of m. For this four-frame tracking algorithm, six pairs of (θ, b) coordinates are calculated in the Hough space. When those six points are spatially close, the pair constitutes a possible vector.

The angle and intercept pairs are then fed into an adaptive resonance theory (ART-2) neural network (NN), one at a time (Carpenter and Grossberg, 1987). The ART-2 NN is a network that self-organizes stable recognition codes (clusters) in real time in response to arbitrary sequences of input patterns. In a gross description, an ART-2 NN is composed of an input layer, a comparison layer, a recognition layer, and the output clusters. In our case, the ART-2 NN classifies the input data (the (θ, b) pairs) into clusters having similar characteristics, i.e., similar values of θ and b. Each new (θ, b) pair fed to the input layer is compared and tested to see if it fits into an already existing cluster (vigilance test). The vigilance test is passed if the pair, say, (θ_k, b_k) satisfies the following equation

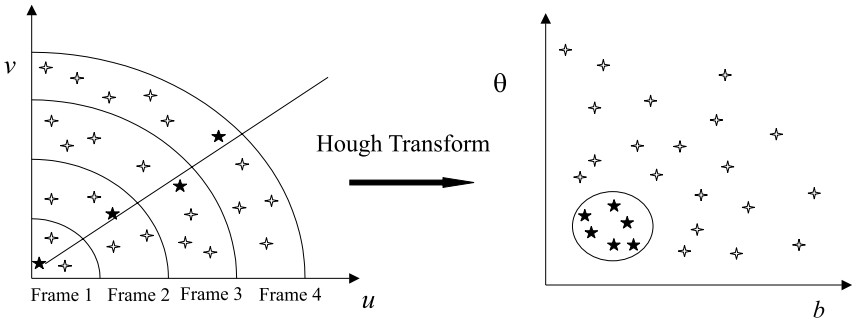

Fig. 4. The Hough transform. Images of the same tracer particle having an alignment property in consecutive frames are mapped to a tight area in the Hough space.

$$\left(\frac{\theta_k - \theta_l}{\theta_r}\right)^2 + \left(\frac{b_k - b_l}{b_r}\right)^2 = 1.0, \tag{3}$$

where (θ_l, b_l) is the centroid of the testing cluster, and (θ_r, b_r) is a fixed pair representing the vigilance parameters. The values of these two parameters depend on the specific problem, and are obtained from values of the Hough transform, from the experimental data. If the vigilance test is passed the pair (θ_k, b_k) is included in the cluster, and a new centroid is computed through

$$\theta_l^{\text{new}} = \frac{\theta_k + n\theta_l^{\text{old}}}{n+1}, \tag{4}$$

$$b_l^{\text{new}} = \frac{b_k + nb_l^{\text{old}}}{n+1}, \tag{5}$$

where n is the number of elements already in the winning cluster l. In this way, each winning cluster is updated to take into consideration new members. If the vigilance test fails, a new cluster with centroid (θ_k, b_k) is formed. The process is repeated for every single pair (θ, b) determined through the Hough transform.

The output of the neural network is clusters for all those combinations of particles having similar angle and intercept pairs. After the clustering process, the possible combinations of particles that may form a pathline undergo a filtering process, for each cluster. This filter selects the particle combination that produces a vector that best matches the characteristics of the flow, by computing an average velocity and acceleration, and their respective associated errors. The flow characteristics help to determine which group of seed particle images are closer to the actual flow, because it determines both the area and preferred direction that a particle in frame 1 needs to look to match candidates in the next three frames. In addition, computational time is reduced. Knowledge of flow characteristics is also used by other tracking techniques, including the cross-correlation (Keane and Adrian, 1992) and spring model (Okamoto et al., 1995). However, in these techniques a group of particles needs to be present in a similar pattern from frame to frame to determine the best possible vectors.

The reconstruction of the 3D flow field is performed using a stereoscopic technique. Before the three components of any tracer particle can be determined, it is necessary to obtain information of the same particle from two different views. The 2D vectors were matched from the vectors obtained by the PIVC camera and the right (PIVR) camera, see Fig. 1(b), and by the PIVC camera and the left (PIVL) camera. The criteria to match velocity vectors from the stereo images are described next.The process started by selecting a 2D vector tracked by the ART2 NN from four consecutive images acquired by the PIVC camera. Then, the corresponding match vector was looked for among all the 2D vectors similarly tracked from images acquired, for example, by the PIVR camera. Thus, for this camera, the image coordinates are u_{R} and v_{R}. Similarly, for the PIVL camera, the image coordinates are u_{L} and v_{L}. The x, y, and z are the world coordinates. It is considered that a vector from the PIVR camera, for example, is a possible match with a vector of the PIVC camera when the axial coordinates of the start and end points of both vectors have similar z coordinate values. Consequently, the difference in magnitude of the velocity in the v-direction, Z-direction, is less than a given tolerance ϵ_z, that is,

$$|\Delta v_{\text{C}} - \Delta v_{\text{R}}| \leqslant \varepsilon_z. \tag{6}$$

Note that this is a direct consequence from the three PIV cameras being positioned such that the v-coordinates coincide in all of them, and consequently z is already known from the calibration. We, then, considered only the starting point of the vector, and x was computed directly from u_C, from the calibration data. This is due to that the image plane of the PIVC camera was parallel to the XZ world plane. There was a range in which y (the depth) must fall for every value of x. Thus, the matched vector in the image from the PIVR camera needed to be searched in a region, since u_R is function of y. Consequently, u_R should in a bounded region be given by

$$u_{Rmin} - \varepsilon_x \leqslant u_R \leqslant u_{Rmax} + \varepsilon_x. \tag{7}$$

We found that there was practically a linear relation between y and u_R; and $y$and u_L, as a consequence of the long focal length of the cameras (high zoom). This facilitated determining the boundaries of the search region, (u_{Rmin} and u_{Rmax}) and (u_{Lmin} and u_{Lmax}). More details of stereo vector matching are given by Ortiz-Villafuerte (1999).

All velocity vectors tracked from images acquired by the PIVR and PIVL cameras that satisfied the two previous conditions (i.e., Eqs. (6) and (7)) were considered candidate match vectors to the originally chosen vector from the PIVC camera. The *epipolar geometry* (Ayache, 1991; Maas et al., 1993) constraint was applied to every candidate vector to determine the real match vector, if any. In brief, the epipolar geometry constraint indicates that for any point on an image, its corresponding match point on the corresponding stereo image lies on a line crossing the stereo image. However, the precise location of the matching point on the line is unknown. The epipolar geometry is a very important condition used in robot and computer vision for the computation of the third coordinate from two 2D scenes. The interested reader is referred to Ayache (1991) for a full description, and computational aspects. The epipolar constraint was employed here as follows. The distances between each of the component start and end points of the candidate velocity vector and its corresponding epipolar line were calculated. The candidate vector whose component points are closest to the epipolar lines was considered the winning vector. In the case of two or more vectors having one point close to its epipolar line, but the other point far away, the vector whose magnitude in the v-component was closest to the reference vector from the PIVC camera was considered the winning vector.

It should be noted that a matching process of the 2D vectors was performed, and not for the individual particles. Therefore, the possibility of mismatching particles was greatly reduced. Also, there was a significant reduction of computational time, since there was no need to go through the process for all the particles for each of the images. Actually, the starting point of the vector was only used to search for candidate match. Obviously, when there was zero or one candidate vector, the epipolar constraint was not computed. Each pair of cameras tended to match more vectors on its respective side; that is, the camera pair PIVC–PIVR matched vectors mostly from the center of the image to its right, and similarly with respect to the left side for the camera pair PIVC–PIVL. In this way, 3D vectors were obtained for most of the viewing volume. In this study, the camera pair PIVL–PIVR was not used for matching.

In summary, the stereoscopic reconstruction process yielded 3D vectors that satisfied:

(a) the tracer particles presented an alignment in four consecutive image frames;

(b) the three image vectors did not deviate far from the local mean velocity and acceleration;

(c) the starting and ending points of each velocity vector had the same z coordinates, in the images acquired by each of the PIV cameras, and consequently, the axial velocity component, w, of the tracer particles had the same value;
(d) an image vector from the PIVR or PIVL camera that was a possible match to a given vector from the corresponding PIVC camera image, was to be found in a bounded region, which depended on y; and
(e) the epipolar constraint.

Those 2D vectors not satisfying the above requirements were considered orphan vectors (vectors without a match) and were disregarded for the later data analysis. Further, repeated vectors were also filtered out. The above five criteria demonstrate the reason for obtaining a total low number of 3D vectors. On the other hand, the quality (real matches among images from cameras at different view angles) is greatly enhanced.

To compute the 3D position of a particle, the (x, y, z) world coordinates of the particle, the perspective projective equations, Eqs. (1) and (2), were used, with information from two cameras. The resulting system of equations is overdetermined, and can be solved by least squares. A schematic showing the whole process from tracking 2D vectors to the 3D position reconstruction is presented in Fig. 5. The spot images shown in Fig. 5 are only small parts of an actual 2D flow field images acquired by the cameras. The matched vectors were then combined for a certain bubble rising trajectory, as is explained later in the section of experimental results and discussion. The 3D liquid velocity vectors of the test volume are also presented in Fig. 5. This liquid velocity field is for a bubble trajectory close to the centerline, 16.67 ms after the bubble had exited from the test volume.

5. Accuracy of measurements

Flow visualization techniques cannot resolve the whole range of time and length scales due to camera resolution and a limited frame rate. In our measurements, limits on the minimum and maximum range of the 2D tracks were set after analyzing many of the acquired pictures. It was found that 4 pixels $\leqslant u \leqslant$ 25 pixels (38.8 pixels/mm), and 4 pixels $\leqslant v \leqslant$ 40 pixels (19.6 pixels/mm) were the optimum values for the 2D tracking of the velocity vectors. For the 60 Hz framing rate, the velocity ranges in the u and v directions were 6.2 mm/s $\leqslant V_u \leqslant$ 38.7 mm/s, and 12.3 mm/s $\leqslant V_v \leqslant$ 122.7 mm/s, respectively. The uncertainty in the velocity measurements is a direct consequence of the combination of errors from three main sources. These are the localization of the centroid of the seed particle images and their displacements in the 2D images, the determination of the 3D position of the seed particles, and the uncertainty of how faithfully the tracer particle follows the actual fluid motion.

An estimation of how close the seed particles follow the flow pathlines, or how fast the seed particles respond to the flow fluctuation and changes, can be calculated utilizing the particle Stokes number. This parameter can be calculated as the ratio of the relaxation time of the seed particle to the characteristic time of the flow. The particle relaxation time τ_p, also known as the momentum or velocity response time, is the time needed by a seed particle to reach $e^{-1}U$, if the particle was initially at rest. Here U is the fluid velocity. τ_p can be computed from

$$\tau_p = \frac{(2\rho_p + \rho_f)d_p^2}{36\mu_f}, \tag{8}$$

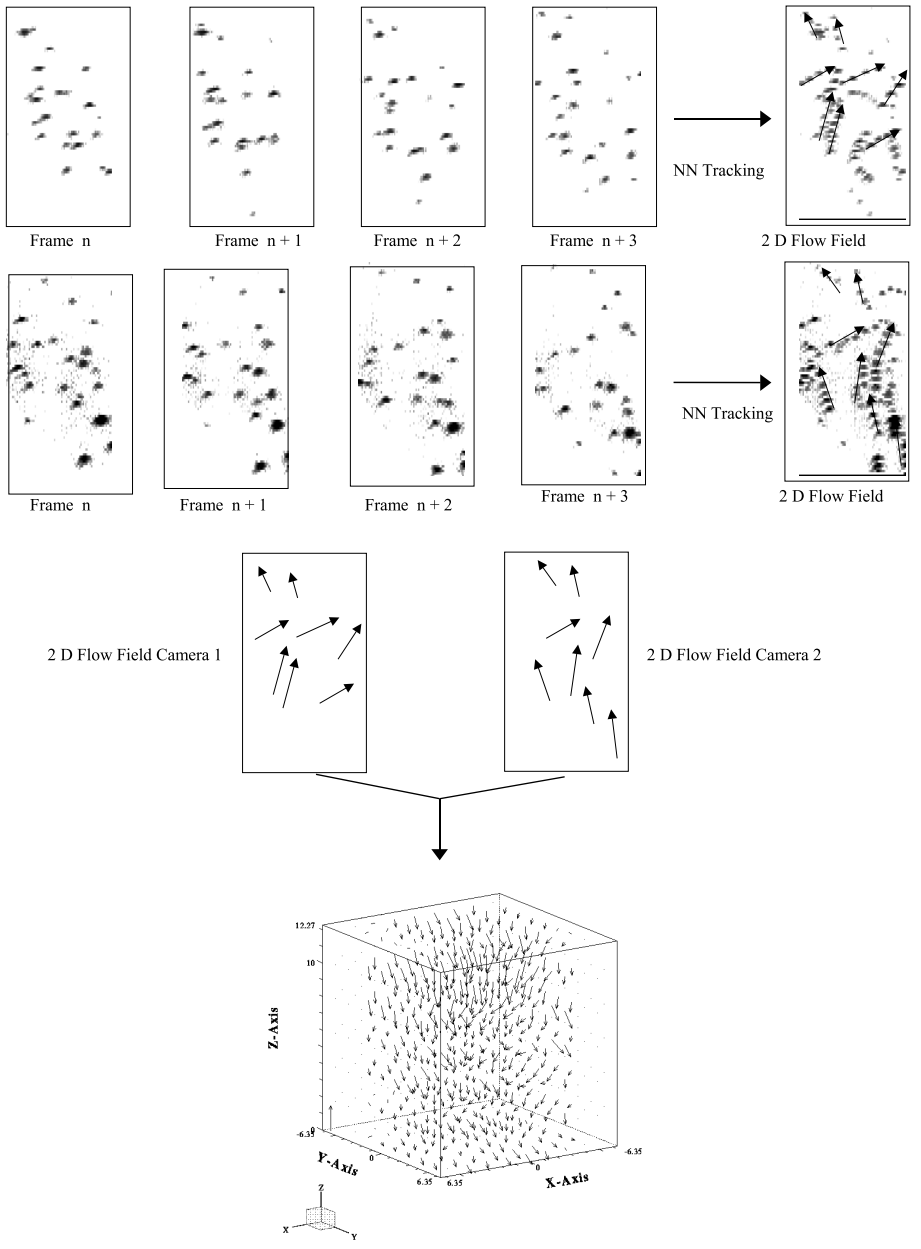

Fig. 5. Three-dimensional stereoscopic reconstruction technique.

where the subscript p refers to particle properties, and f to the fluid properties. In our case, the relaxation time of the seed was calculated to be 140 μs. The fluid time scale, τ_f, is the time needed by the fluid to be advected a characteristic length L, that is,

$$\tau_f = \frac{L}{U}. \tag{9}$$

For the characteristic time of the flow, we used an equivalent diameter of the bubble of 3 mm as characteristic length, and the maximum measurable liquid velocity. The resultant time was 24 ms. Then, the Stokes number, τ_p/τ_f, was calculated to be 5.72×10^{-3}. Therefore, the 40-μm seed particles followed closely the fluid motion changes, and therefore, did not significantly contribute to the total error.

Adrian (1986) determined the error associated in localizing the 2D particle–image centroids, and their displacements between two or more consecutive frames. For our continuous laser, the uncertainty in the time interval results from the laser pulse width. In our case, it was 250 μs, compared to the characteristic time of the flow of 24 ms, hence it had a negligible error on the velocity values. The error in locating the centroid displacements depends on the optical parameters of the camera, focal length of lenses, laser light distribution profile and wavelength, and the algorithm for locating the particle–image centroid. Our algorithm has a subpixel accuracy of about 95%, and the magnification of the system used in the experiment allowed for even better accuracy. The error in determining the centroid displacement was less than 1% of the total error.

The main error source in our velocity measurements was the calculation of the three world coordinates of the seed particles. The calibration was the main source for this type of error, since it was done by using a least squares method, as explained before. To calculate the error associated to each world coordinate, we used Eqs. (1) and (2) to compute the 3D positions of the calibration points. Then we compared the computed values against their known positions. The root mean square (r.m.s.) error in each direction was 25 μm in X-direction; 96 μm in Y-direction; and 23 μm in Z-direction. In terms of the velocity, the r.m.s. error for each component was: 1.6 mm/s in the x-component; 5.8 mm/s in the y-component; and 1.4 mm/s in the z-component. These values were estimated for a framing rate of 60 Hz. Thus, the error associated with small flow velocity less than 5.8 mm/s was significant.

To compute the error associated to every component of the vorticity vector, $\boldsymbol{\omega}$, calculations of the gradients and associated uncertainties are also required. The central finite difference scheme was employed for the calculation of the velocity gradients in all directions. The error for the vorticity vector components was estimated to be 10.3 Hz in the X-direction; 3.7 Hz in the Y-direction; and 10.4 Hz in the Z-direction.

6. Results and discussion

Eighty-one sets of data were acquired in this experimental investigation. Each set consisted of 27 frames. Fig. 6 shows the distribution of the projection of bubble centroids for the experiment duration on the horizontal XY-plane, when the bubble is present in the viewing volume. This figure clearly shows the anisotropy of the bubble paths as they rise. The bubbles were released near the pipe center. Saffman (1956) noted that bubbles with spherical equivalent diameter d_b between 2.0 and 4.6 mm mostly traveled in a zigzag trajectory just after release, without any preference for a particular plane. However, if the bubble experienced sufficiently strong external disturbances, the trajectory changed from zigzag to spiral, but not the opposite. In principle, an undisturbed bubble ensures an isotropic distribution of the bubble centroids projection on the XY plane, if a large enough number of bubbles are considered in the statistical analysis. In our experiments, the bubbles were released under the same conditions, but their volume and shape

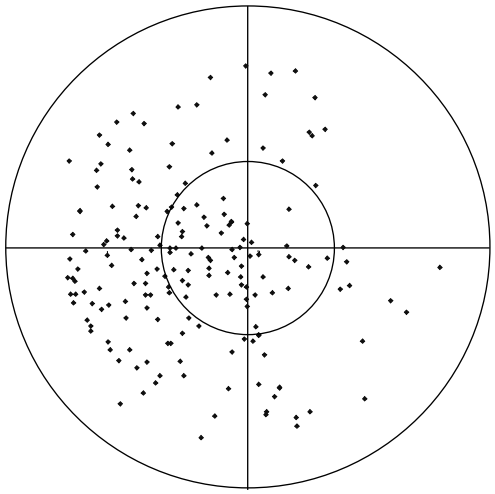

Fig. 6. Distribution of the bubble centroids for the whole experiment on the XY plane. The anisotropy of the bubble paths during rising should be noted. The bubbles were released near the pipe center.

presented variations. Such differences among the bubbles lead to different velocities. We believe that the anisotropy of the bubble paths, shown in Fig. 6, in the XY plane is due mainly to the mixing of zigzag and spiral trajectories, plus the bubble rocking motion. Further, the spiral trajectory was more probable to occur because of the bubble/wall interaction (the external disturbance), which limits the amplitude of the lateral movement, and increases the rocking motion of the bubbles. In addition, any tiny deviation between the vertical and the pipe axis may cause the observed preferred pattern.

Fig. 7 shows an overlay of four consecutive frames in which a rising bubble was present in the viewing volume, and the top view (XY plane) of the 3D reconstruction of three of the bubble images. The image of the bubble when entering the test volume, the bottom bubble image, could not be 3D reconstructed since no information of its lower part was available. The bubble images in Fig. 7(a) were acquired by the PIVC camera, so it presents a view of the XZ plane. The nodalization scheme for the bubble location in the viewing volume is also illustrated in Fig. 7. The axial nodalization consisted of four segments, each with a size of $\Delta Z_b = 3.07$ mm, as shown in Fig. 7(a). The horizontal plane was divided in five regions, as shown in Fig. 7(b). The circle segment number 1 is at the center of the pipe, with a radius of 2.25 mm, and the annulus region was divided into four segments, 2, 3, 4, and 5. The number of cells of the nodalization used to determine the location of the bubble was 20 (four vertical $\times$ five horizontal). For the liquid-phase data, the measurement volume was divided into a 3D grid of $9 \times 9 \times 6$ in the X-, Y-, and Z-directions, respectively. Out of the total number of the cells (486), only 294 were inside the pipe. The size of the node for ΔX and ΔY equals 1.41 mm and $\Delta Z = 2.05$ mm. Fig. 8 presents the nodalization used for the liquid phase.

An average of 900 vectors per time step was used to perform the averaging process. The average number of vectors used for the statistical analysis increased to about 1200 vectors per time step after the bubble left the viewing volume. The averaged flow field was then interpolated. Although several options exist to perform interpolation, most of them yield unsatisfactory results when only

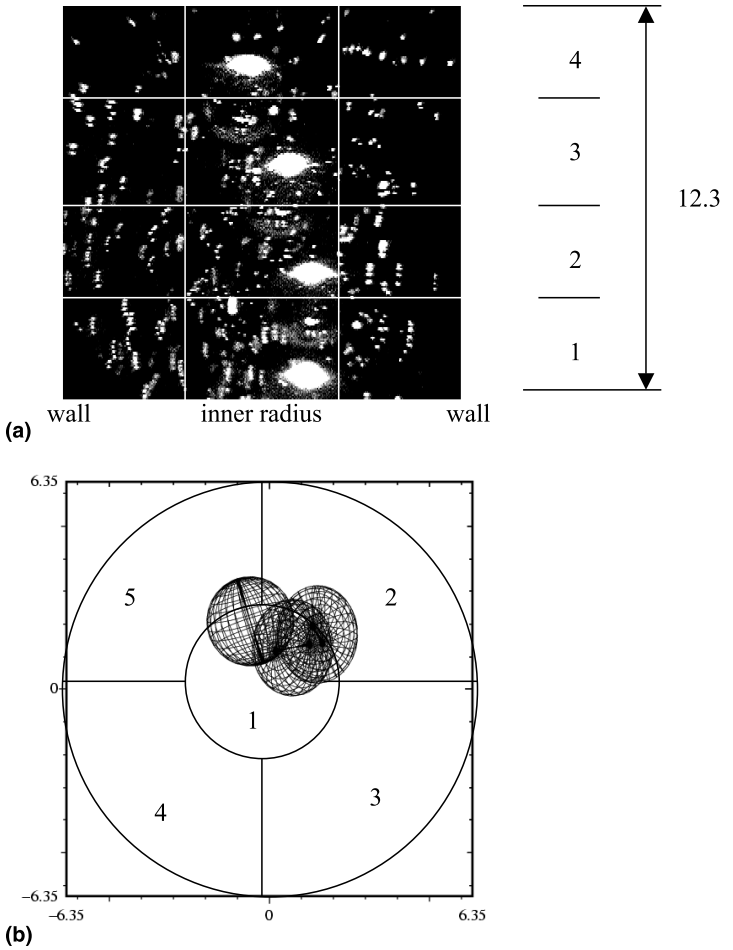

Fig. 7. Typical overlay of four consecutive frames when the bubble is present in the viewing volume. The nodalization of the gas phase is also included. (a) Image from center camera (XZ plane), and axial nodalization. (b) Top view (plane XY), and nodalization on the XY plane. Dimension in mm.

sparse data is available. The interpolation algorithm employed here is based on the Hardy scheme (Hardy, 1990; Blanchat, 1991), which performs a bi-quadratic interpolation. Bi-quadratic interpolations in fields with sparse data have been successfully employed in 3D domains by Hardy (1990) and Adamczyk and Rimai (1988). The error associated with the interpolation for each velocity component was always less than that due to calibration, therefore, its contribution to the total error was insignificant.

In our analysis, the data sets were divided into groups having similar bubble trajectories. A similar bubble trajectory was that in which the bubble, in its rising path within the viewing test volume, passed through the same region (locations) in at least three or four sequence frames. An example of bubble trajectory 111 is depicted in Fig. 7, which clearly shows that bubble trajectory was not a straight path. Fig. 7(a) shows that the pipe is divided into central and close to pipe wall regions. Fig. 7(b) indicates that the centers of the bubble are located in the segment number 1. The

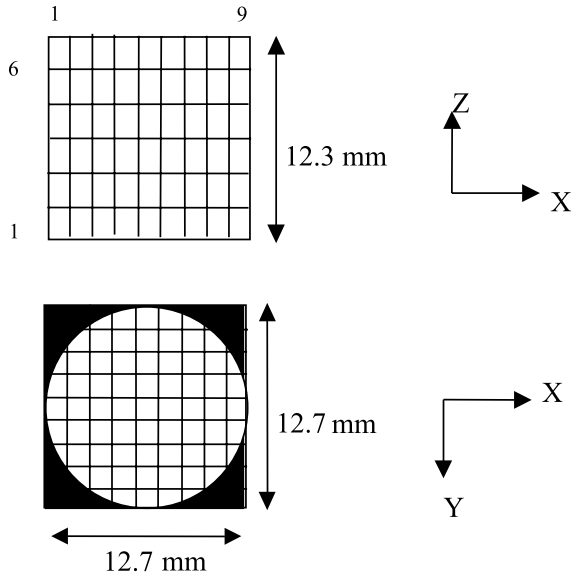

Fig. 8. Nodalization for the liquid phase.

distribution of the various trajectories within the test volume, for our experiment was as follows: 17.3% of the bubble paths followed trajectory 111; 2.5% with trajectory 222; 3.7% with trajectory 333; 19.8% with trajectory 444; and 18.5% of the trajectories were 555. The rest of rising paths were a combination of trajectories. By combining the bubble data for a specified trajectory, we obtained an average flow field, at each instant in time.

The conditional average velocity field was obtained according to the following equation:

$$\bar{\mathbf{u}}(x,y,z,t_b) = \frac{1}{N}\left\{ \sum_{i=1}^{N} \mathbf{u}_i(x,y,z,t_b) \middle| \begin{array}{l}\text{specified}\\ \text{bubble}\\ \text{trajectory}\end{array} \right\}, \tag{10}$$

where N is the total number of vectors that fall in a nodal liquid volume for all similar bubble trajectories, at each instant in time with respect to the first appearance of the bubble in the viewing volume, t_b. In our ensemble average, we did not consider the spiral turning (right turning or left turning) direction of the rising trajectory, nor the rocking motion. Although the ensemble average obscures the details of the flow surrounding the bubble, it allows for direct comparison with average values obtained with point measurement techniques. Computational fluid dynamic programs used in nuclear safety analysis are based on the averaged Reynolds equations, and do not take into account bubble trajectory and turning direction. Only the scalar quantity of void fraction distribution is considered in the formulation. It is important to differentiate between the "real" turbulence and the deviation from the mean values. Note that the ensemble average considered in this study contains an average over space. To determine the turbulence it is necessary to average the flow field for a fixed position of the bubble and similar orientation. For a given bubble position, the distance between the bubble surface and the pipe wall is also another important factor that should be considered. In this study, a phase-resolved ensemble was

achieved. In our phase-resolved experiments, for every individual image with full-field velocity measurements, the position of the bubble is determined. A reconstruction of the mean flow field and its fluctuations as a function of the bubble location and trajectory was obtained. In this investigation, we have preferred to perform the average based on the rising bubble trajectory. This allows us to study the wake flow when the bubble is within the viewing volume, and after the bubble departure. However, we cannot separate the contributions of the turning direction of the bubble and the bubble rocking motion to the total turbulence.

Fig. 9 shows the kinetic energy per unit mass of the liquid, in mm^2/s^2, of the mean flow field and the turbulent flow field, during the whole measurement, for three different bubble trajectories. Note also that the turbulent kinetic energy is the variance of the mean kinetic energy. In Fig. 9, time step 0 ($t_p = 0$ms) corresponds to the first frame in which the bubble appears in the viewing volume. Subscripts b, p, and a, refer to the time before the bubble arrival to the viewing volume,

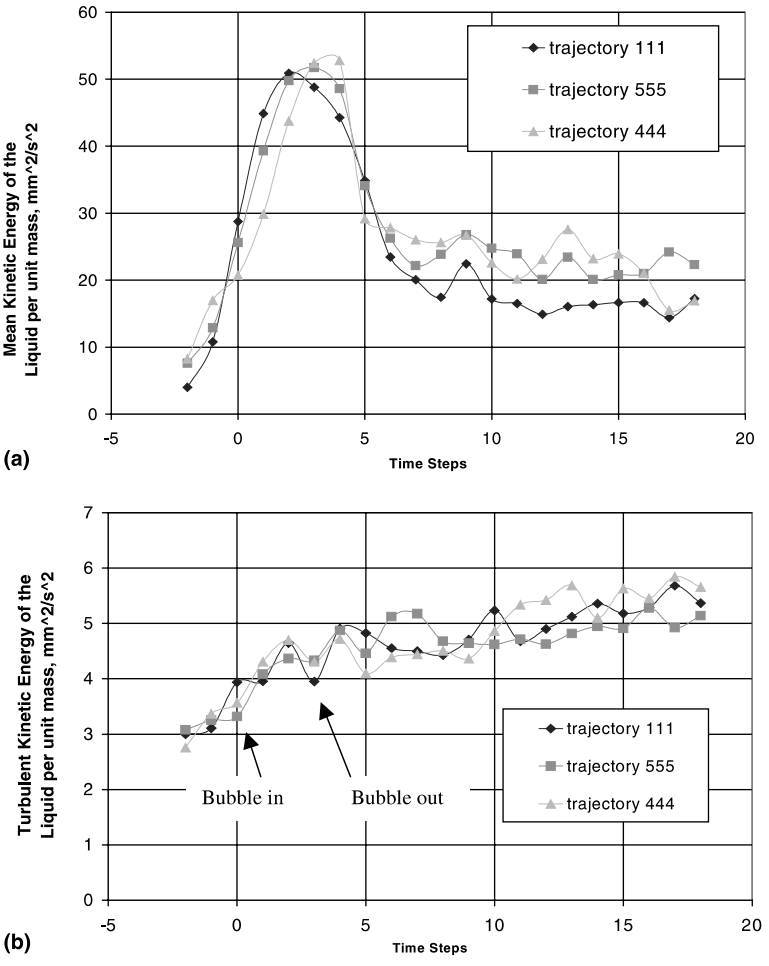

Fig. 9. Kinetic energy of the liquid per unit mass in mm^2/s^2, for three different bubble trajectories, at each time step: (a) mean, (b) turbulent.

bubble presence in the viewing volume, and the time after the bubble departure from the viewing volume, respectively. This figure also demonstrates that the influence of the bubble in the viewing volume is first observed at $t_b = 33.33$ ms ($t_b = 2\Delta t$, where $\Delta t =$ framing time step). The three curves in Fig. 9(a) show a sharp increase in the liquid motion in the viewing volume at $t_p = 16.6$ ms ($t_p = \Delta t$). The maximum of the kinetic energy for the trajectories 444 and 555 is reached at $t_p = 50.0$ ms ($t_p = 3\Delta t$). These bubble trajectories are close to the wall. However, the maximum for trajectory 111 (bubble rising along the pipe core) is reached at $t_p = 33.3$ ms ($t_p = 2\Delta t$). A sharp decrease of the kinetic energy in the volume can be seen at $t_a = 33.3$ ms ($t_a = 5\Delta t$). This indicates that the primary wake has totally departed the viewing volume. Trajectories 444 and 555 have higher values of the mean kinetic energy than trajectory 111, which indicates a stronger interaction of the bubble wake left in the volume. This increase in the contribution of the kinetic energy is due to the pipe/wall interaction. Observe that for all trajectories, once the bubble has departed, the turbulent kinetic energy reaches about 30% of the values of the mean kinetic energy. This is due to the decay of the mean flow because of viscous effects and wall friction. On the contrary, the turbulent part of the velocity field slowly increases due to the influence of the bubble wake (Fig. 9(b)). Ellingsen and Risso (1998) found that the vortex street behind a rising bubble extends a distance of more than twenty-five d_b. In our case, the observed distance is equivalent to sixteen d_b, considering an average bubble speed of 190 mm/s. Longer measurement duration of about 0.5 s is needed to observe the decrease of the turbulent kinetic energy within the viewing volume.

A comparison of the influence on the flow field of the bubble trajectories close to the pipe wall, as trajectories 444 and 555, with the central region trajectories, as 111, was performed. The characteristics of the mean flow indicate that for trajectory 111 the bubble influence reaches as far as an average distance of two d_b in front of (downstream) the bubble, as shown in Figs. 10(a) and (b). The bubble's near wake effect extends about three d_b behind (upstream) of the bubble, as delineated in Figs. 10(c) and (d). The liquid tilted velocity vectors toward the pipe center colliding in the bubble's rear determine the length of the primary or near wake. This indicates a closed wake, although the details of the internal flow circulation cannot be resolved in this measurement, because of the low nodalization resolution and the smearing effects of averaging process. When a bubble is flowing within the pipe central region, practically all of the liquid flow is restricted to a space of about one and half d_b between the bubble boundary and the pipe wall. To preserve continuity, the flow accelerates as a consequence of the reduction of the available flow area. It is observed that the liquid flowing around the primary wake, and that being redirected from the pipe wall collide at the end of the closed wake, near the pipe center. This flow collision behavior has similarity with the collision of opposing jets, creates a zone in which the velocity of the liquid flowing upstream is reduced. We have denoted such deceleration zone as "flow barrier", and it can be seen in Figs. 10(c) and (d).

Bubble trajectories close to the pipe wall (as trajectories 444 and 555) presented a significant difference on the influence of bubble upstream and downstream on the flow field in a comparison with the trajectory 111. The downstream influence reaches an average of three d_b. This can be explained by noting that a portion of the liquid flow has to pass through a very narrow area between the bubble and the wall. This flow thus should greatly accelerate. However, the momentum transfer from the bubble to the liquid is not enough to overcome the wall friction and to result into a high acceleration of the flow. Consequently, the liquid is pushed in front of

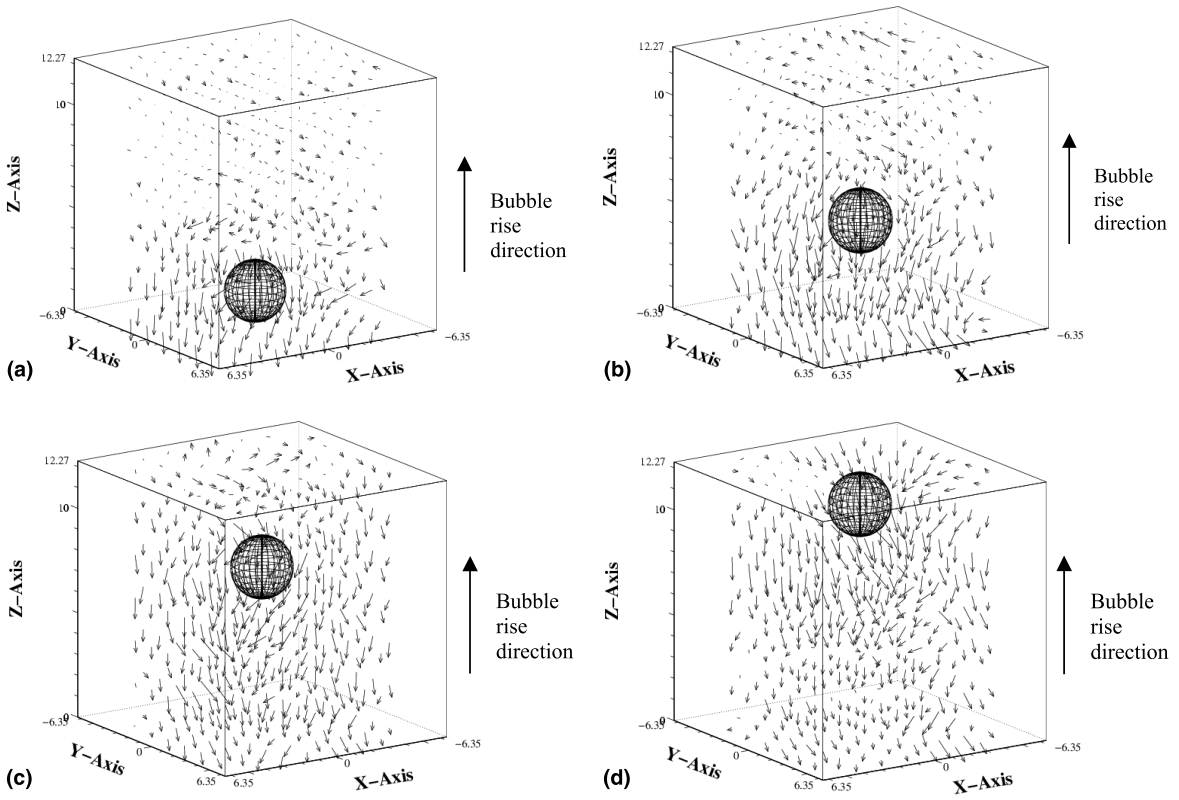

Fig. 10. Velocity fields for bubble trajectory 111. (a) $t_p = 0$ ms, (b) $t_p = 16.7$ ms, (c) $t_p = 33.3$ ms, and (d) $t_p = 50.0$ ms.

the bubble. This liquid relocates larger adjacent liquid layers. The downstream bubble influence, therefore, reaches a greater distance when compared to a bubble rising in the center of the pipe. The length of the primary wake extends to an average of three d_b behind the bubble. The primary wake region is smaller than that for a bubble with trajectory 111 and is distorted. The flow at a radial distance of more than two d_b far from the bubble is practically undisturbed and has almost constant flow direction. This liquid flow is reduced as it gets closer to the pipe wall. The flow barrier is generated once again, but it is restricted to a volume about the size of the bubble. The maximum liquid kinetic energy, which is obtained at different time (as displayed in Fig. 9(a)), is due to the various sizes of the flow barrier for different bubble trajectories.

The Reynolds number of the bubble Re_b ranged from 350 to 700, based on the total speed of the bubble and the mean spherical diameter of the bubbles. The speed of the bubble is given by $U_{bT} = \sqrt{u_b^2 + v_b^2 + w_b^2}$, where w_b is the axial (rise) bubble velocity, and u_b and v_b are velocity components in the X- and Y- directions, respectively. Clift et al. (1978) showed that, at this Reynolds range, bubbles freely rising in stagnant water in an infinite medium have oscillations in the rising path and bubble shape. The shape changes from spherical to ellipsoidal, although not necessarily symmetric. The bubble trajectory is either spiral or zigzag, depending on the bubble volume and external disturbances at the moment of release (Saffman, 1956). Further, bubble

rocking motion can be expected. In our experiments, both the spiral and zigzag paths were observed. The rocking motion was also observed.

The relative velocity between the bubble and its surrounding liquid induces shear stresses and high vorticity regions. These vortex structures for two of the vorticity vector components are presented in Figs. 11 and 12. Fig. 11 shows three different YZ-planes of the y-component of the vorticity vector, ω_y, for the four time instants when the bubble is present in the viewing volume. Following the bubble motion, some characteristics of the flow pattern can be observed. Just in front of the bubble ω_y is positive, with values of 1–2 Hz. The size of this vortex region is about one bubble diameter. Areas of negative ω_y, reaching up to -6 Hz, are observed close to both sides of the bubble, with influence extending to the pipe wall. Behind the bubble, just at the rear, ω_y is negative. Surrounding this negative vorticity region, positive vorticity values are observed. The lack of symmetry of the vortex structures is probably due to the elliptic shape of the bubble and the spiraling and rocking motion of the bubble along its axis. Similar vortex structures were also found in the other components of the vorticity vector, even with higher magnitudes. The description of the flow field distribution along the bubble boundary layer, where the velocity

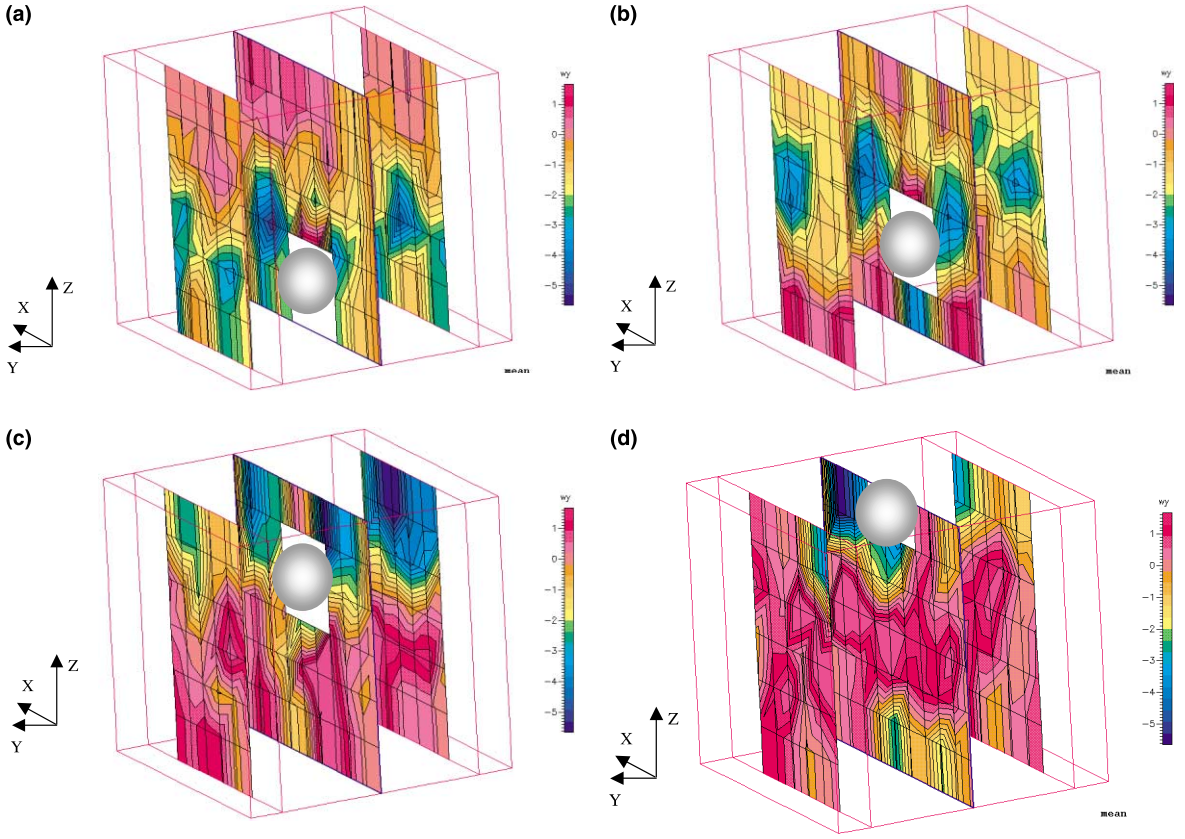

Fig. 11. XZ-planes of ω_y for bubble trajectory 111. (a) $t_p = 0$ ms, (b) $t_p = 16.7$ ms, (c) $t_p = 33.3$ ms, and (d) $t_p = 50.0$ ms.

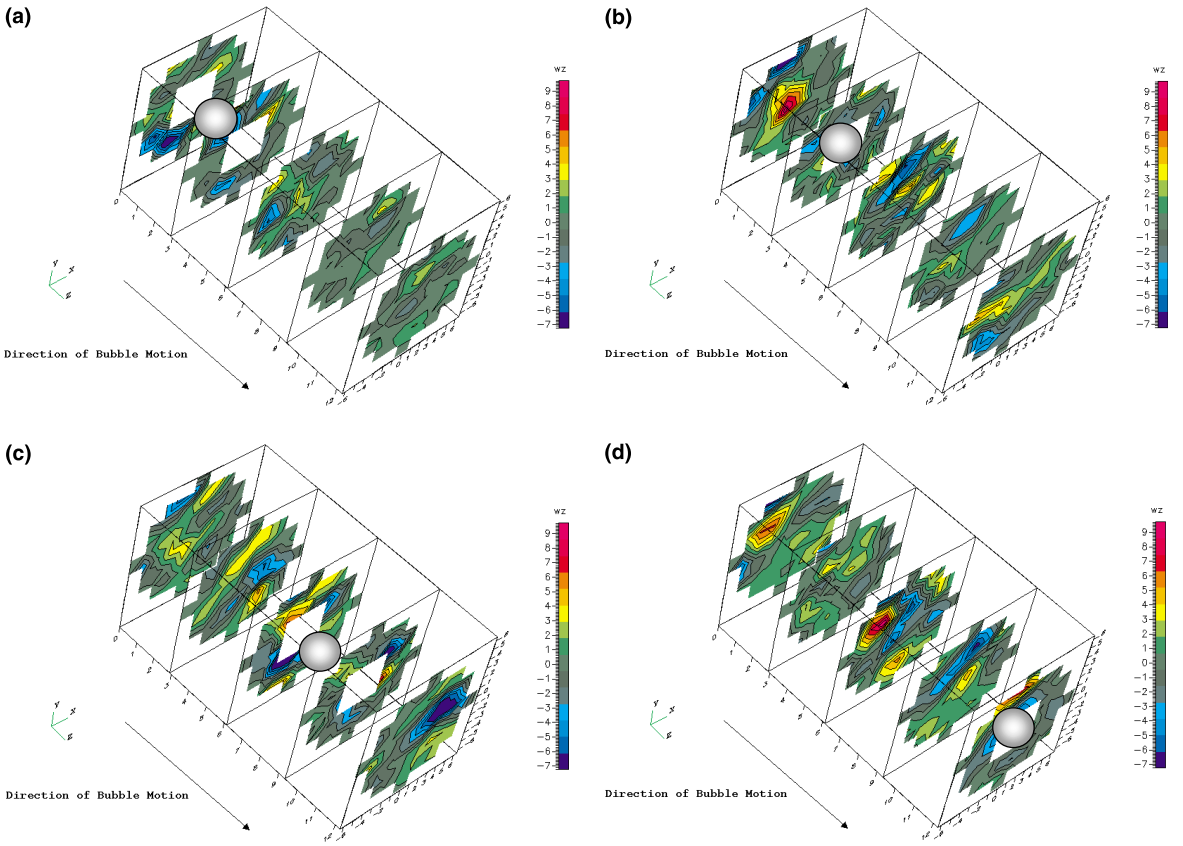

Fig. 12. XY-planes of ω_z for bubble trajectory 111. (a) $t_p = 0$ ms, (b) $t_p = 16.7$ ms, (c) $t_p = 33.3$ ms, and (d) $t_p = 50.0$ ms. The scale in the Z-direction has been doubled to facilitate visualization.

gradients and the vorticity are high, is not provided by our measurements. Fig. 12 presents five different XY-planes of the z-component of the vorticity vector, ω_z, during the bubble presence in the viewing volume. Regions of strong positive and negative vorticity following the bubble as it rises can be observed. Brücker (1999) presented the structure of the wake due to spiraling and zigzagging bubbles. In both cases the vorticity field on the XY plane delineated two counter-rotating vortices. For the case of the zigzagging bubbles, these two vortices were cross sections of the legs of a hairpin vortex structure. For the spiraling bubbles, the two vortices were cross sections of joint streamwise vortex filaments. Our results support such findings. In Fig. 12(d), the two counter-rotating vortices can be clearly seen. Close to the pipe wall, pairs of counter-rotating vortices are also observed in front and behind the bubble. These are generated by shear flow. From the Fig. 11 of vorticity component ω_y and Fig. 12 of vorticity component ω_z, a conceptual schematic depicting the vortex patterns upstream of a rising bubble in our measurements is illustrated in Fig. 13. Schmidl (1999) presented the vector plots and vorticity fields of trajectory 111 for the whole duration of the measurement.

Fig. 14 depicts iso-surface plots of ω_y, for the four time steps when the bubble is present in the viewing volume. In these figures, the positive value is set to 1.4 Hz and the negative to -3.4 Hz.

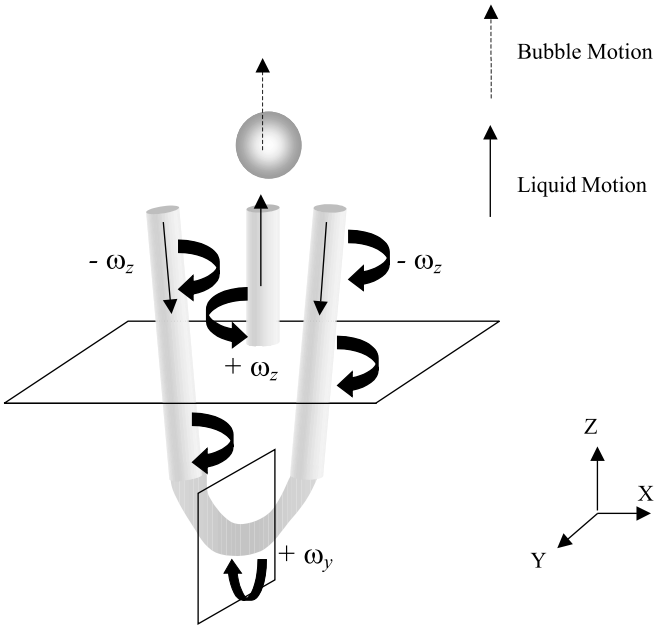

Fig. 13. Conceptual model of the observed vortex pattern upstream of the bubble.

These figures show the regions of vorticity in front of and behind the bubble as it passes through the viewing volume, and delineate the structure of the flow field around the bubble. Fig. 15 depicts iso-surface plots of ω_z when the bubble is present in the viewing volume. Tubes of positive and negative vorticity trailing and leading the bubble can be observed. In these figures the positive value is set to 3.0 Hz and the negative to -3.0 Hz. Discontinuity of the vortex filaments can be observed in Figs. 15(c) and (d). The discontinuities are not only due to the mixing of spiral and zigzag trajectories in the ensemble average operation, but also due to the wall influence. Measurements, carried out by Bosch et al. (1996) on a square cylinder placed near a wall, showed that the wall has little influence on the flow past the cylinder if $G/D = 1.5$, where G is the gap between the body and the wall, and D is the diameter of the cylinder. However, vortices shed from the cylinder surface reached the wall, where they were reflected. These vortex structures, then, interacted with the mean flow and the vortices shed from the other side of the cylinder. This phenomenon is also observed in our experiments. In our measurement, most times $G/d_b < 1.5$, due to the strong lateral motion of the bubble, see Fig. 6 as an example. The interaction of the reflected flow from the wall disturbed the vortex filaments.

Finally, Fig. 16 depicts several pathlines of the liquid flow when the bubble is present in the viewing volume, at $t_p = 0.0$, $t_p = 16.7$, $t_p = 33.3$, and $t_p = 50.0$ ms, respectively. These figures show the complexity of the flow field surrounding the bubble. The path of the continuous phase indicates the motion towards the wall at $t_p = 16.7$ ms and the colliding of the liquid streams along the pipe center at, $t_p = 33.3$ ms. For the bubble trajectories close to the wall, the influence of the wall is stronger than during the bubble motion along the pipe center. It should be noted that by combining data from trajectories 444 and 555, a better statistical analysis could be expected.

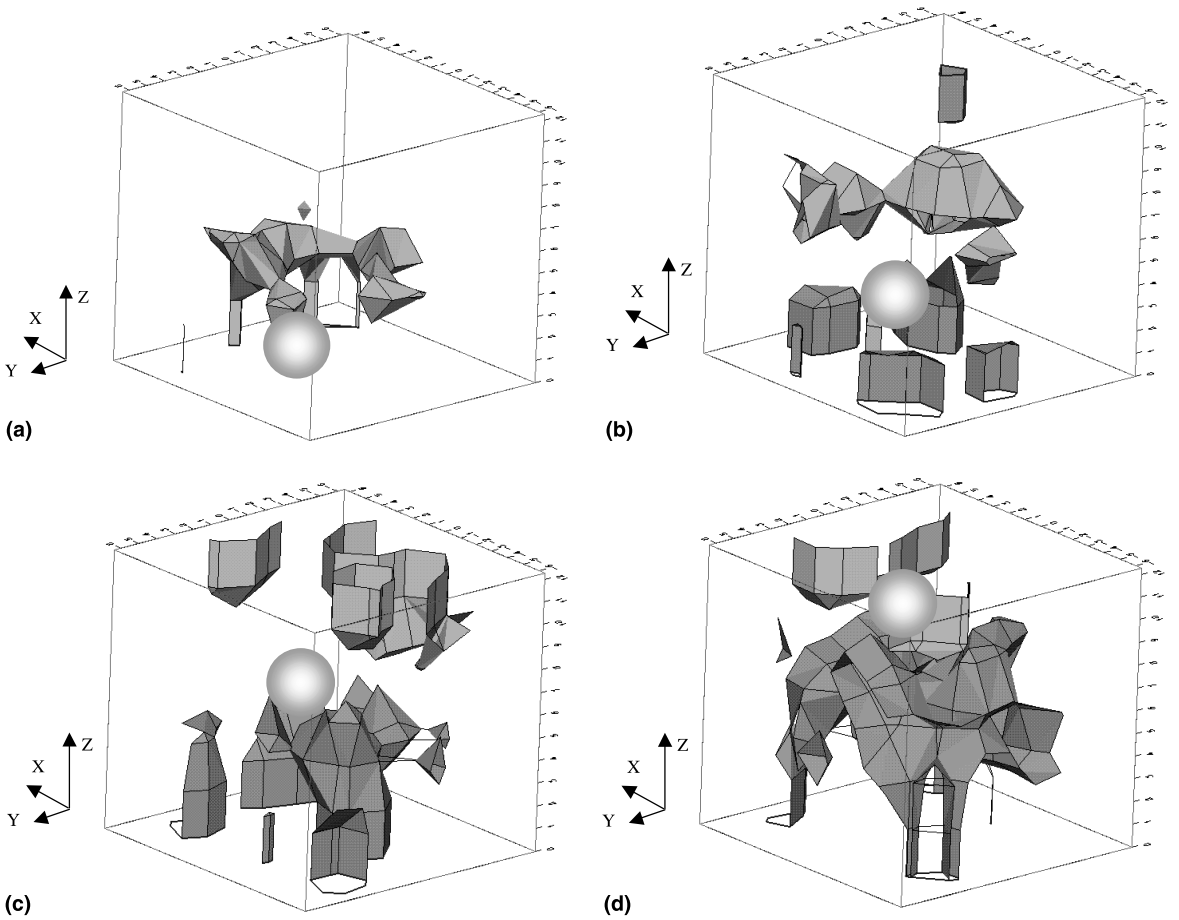

Fig. 14. ω_y iso-surfaces for bubble trajectory 111. (a) $t_p = 0$ ms, (b) $t_p = 16.7$ ms, (c) $t_p = 33.3$ ms, and (d) $t_p = 50.0$ ms. $\omega_y = +1.4$ Hz (dark)/-3.5 Hz (light).

In summary, it seems possible to define four distinct processes in the continuous fluid phase during bubble rise:

- An initial stage, in which the liquid fluid is accelerated upstream of the bubble.
- Liquid impingement on the pipe wall from the accelerated liquid.
- Reflection and deceleration of the liquid flow towards the pipe core, where flow collision occurs.
- During the fourth stage, the liquid flow is redirected towards the wall again, after flow collision at the pipe core region.

As shown before, the disturbances generated by the bubble motion transmit both upstream and downstream of the bubble. When compared to those results with the regions of vorticity, it was determined that vorticity and disturbances zones basically coincide, as expected. Therefore, it is concluded that potential flow can only be correctly applied for regions about two d_b downstream of the bubble, when the bubble rises along the center of the pipe. For the case of bubble rising close to the wall, potential flow can be used three d_b downstream and at least two d_b in the radial

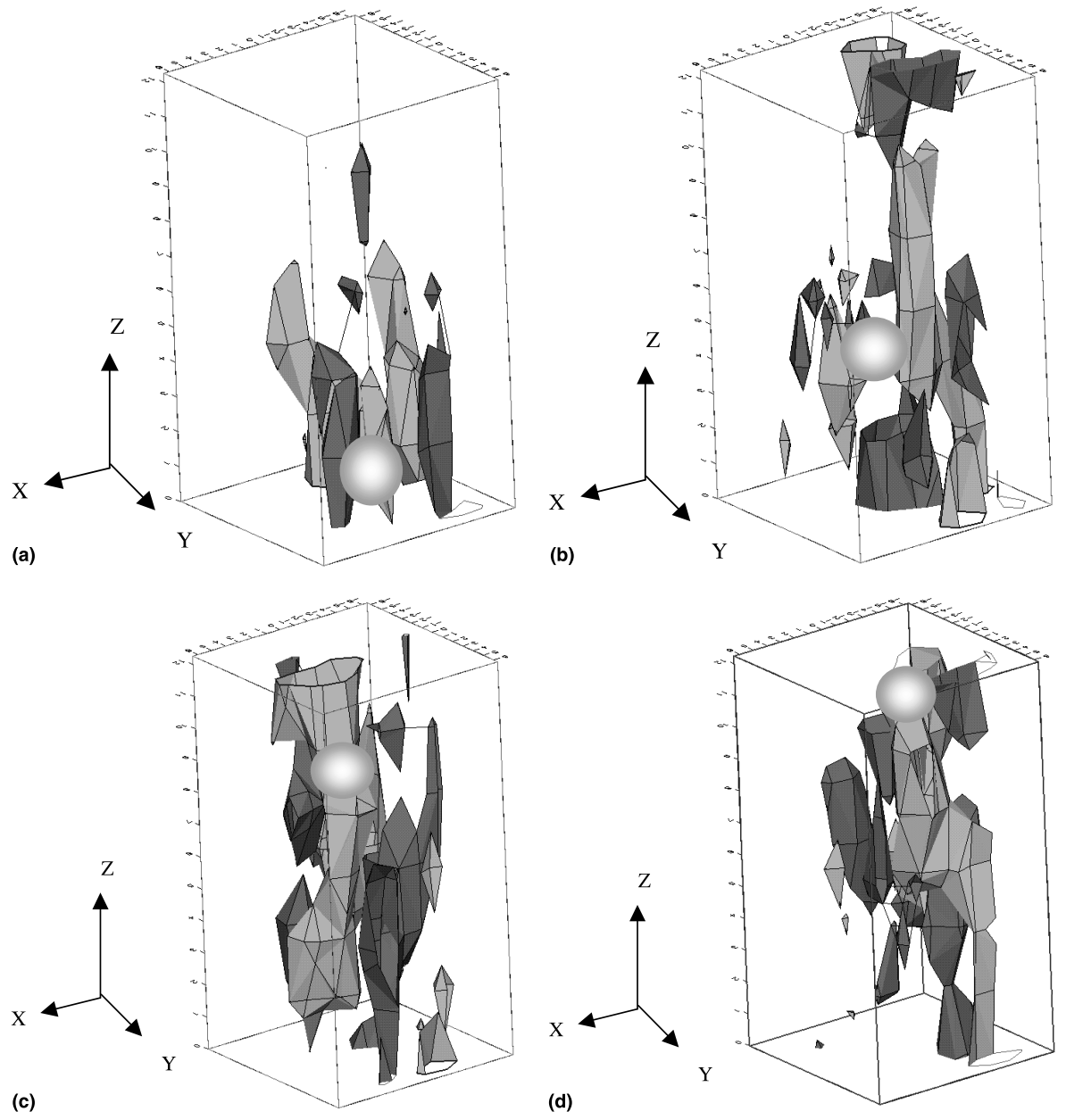

Fig. 15. ω_z iso-surfaces for bubble trajectory 111. (a) $t_p = 0$ ms, (b) $t_p = 16.7$ ms, (c) $t_p = 33.3$ ms, and (d) $t_p = 50.0$ ms. $\omega_z = +3.0$ Hz (dark)/-3.0 Hz (light). The scale in the Z-direction has been doubled to facilitate visualization.

direction far from the bubble surface. Several small zones of high vorticity and turbulence were observed in all the frame images during the period after the bubble departure from the viewing volume. Therefore, potential flow theory validity should be carefully examined when flow description in the wake of a bubble and with a strong wall influence are needed.

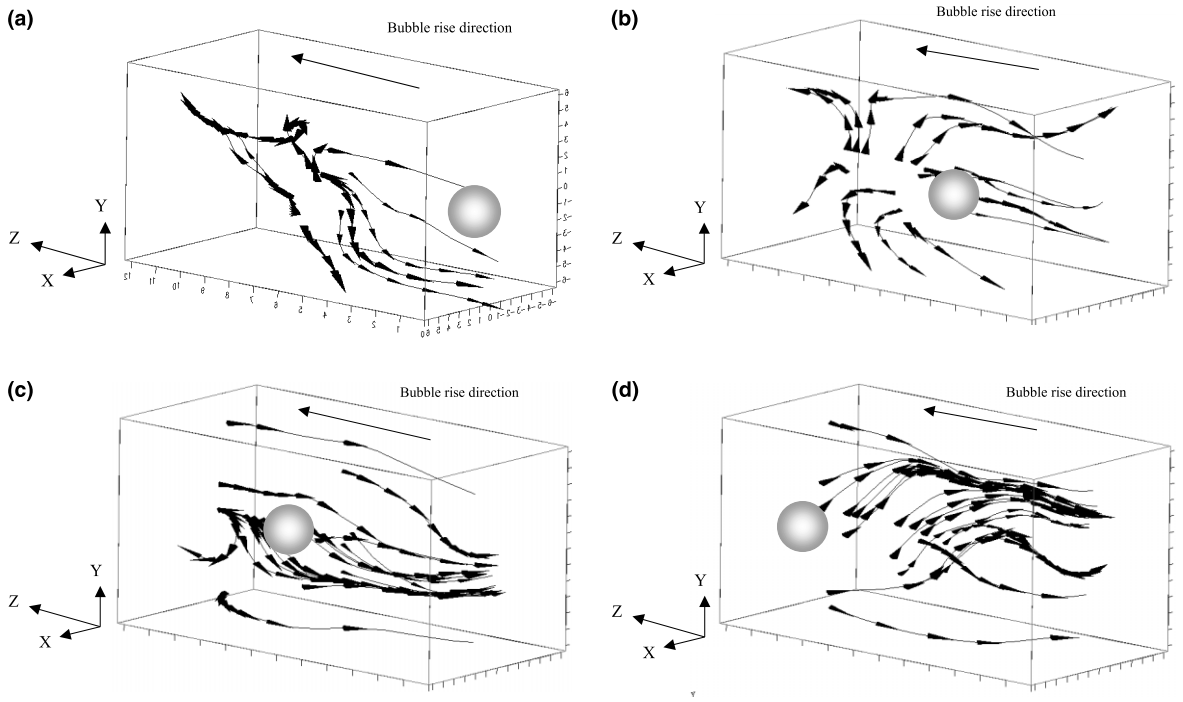

Fig. 16. Some flow pathlines for bubble trajectory 111. (a) $t_p = 0$ ms, (b) $t_p = 16.7$ ms, (c) $t_p = 33.3$ ms, and (d) $t_p = 50.0$ ms. The scale in the Z-direction has been doubled to facilitate visualization.

7. Conclusions

A transient study was conducted for the bubble dynamics of a single bubble rising in stagnant water in a small diameter circular pipe using a whole-volume, three-dimensional particle tracking velocimetry flow measurement system. Accurate measurements of the size, shape, and orientation of the bubble were obtained by complementing the particle tracking velocimetry with a shadow particle image velocimetry technique. The liquid velocity field surrounding the bubble was acquired and the velocity vectors averaged to obtain the time-dependent averaged velocity field. The measurement results show that the mean kinetic energy in the measurement volume reaches its maximum when the bubble is within the volume and during the time in which the primary wake is still in the test volume. The mean kinetic energy is higher for bubble trajectories rising close to the pipe wall. When the bubble rises through the center of the pipe, the bubble-induced liquid motion reaches an average of two bubble diameters downstream, and the length of the bubble wake extends to three bubble diameters. The present study shows that the wall influence on the motion of a freely rising bubble is not limited to restrict the amplitude of the lateral displacement on a zigzag or spiral trajectory. There also exists a strong influence on the surrounding flow of the bubble. A flow barrier is generated at the end of the primary wake, as a consequence of jet-like flow reflected from the pipe wall, decelerating the flow passing through. This flow barrier is larger when the bubble rises in the center of the pipe. Pairs of counter-rotating vortices were found both

behind (upstream) and ahead (downstream) of the bubble. The pairs downstream are generated by shear flow close to the pipe wall; while upstream of the bubble, the vortex pairs are generated by both the wake and wall shear flow. It was also found that potential flow could only be correctly applied for regions two bubble diameters downstream of the bubble, when the bubble rises up in the center of the pipe. For the case of bubble rising close to the wall, potential flow can be applied beyond three bubble diameters downstream and at least two bubble diameters away of the bubble surface in the radial direction. Further, potential flow theory should not be considered to describe the flow in the wake of a bubble at all time, when wall influence is important. A larger number of three-dimensional vectors are required to achieve a spatial resolution capable of minimizing the error introduced by the average operation in the calculation of turbulent quantities. More velocity vectors are needed to describe the flow around a freely rising bubble due to the large velocity gradient, particularly if wall influence is strong.

References

Abdel-Aziz, Y.I., Karara, H.M., 1971. Direct linear transformation from comparator coordinates into object-space coordinates. In: Close-Range Photogrammetry. American Society of Photogrammetry, Falls Church, Virginia, pp. 1–18.

Adamczyk, A.A., Rimai, L., 1988. Reconstruction of a 3-dimensional flow field from orthogonal views of seed track video images. Exp. Fluids 6, 380–386.

Adrian, R.J., 1986. Multi-point optical measurements of simultaneous vectors in unsteady flow. A review. Int. J. Heat Fluid Flow 7, 127–145.

Ayache, N., 1991. Artificial Vision for Mobile Robots: Stereo Vision and Multisensory Perception. MIT Press, Cambridge, MA.

Blanchat, T.K., 1991. Development of pulsed laser velocimetry techniques for measurement of two-phase interfacial drag in a horizontal stratified flow. Ph.D. Dissertation, Texas A&M University, College Station, TX.

Bosch, G., Kappler, M., Rodi, W., 1996. Experiments on the flow past a square cylinder placed near a wall. Exp. Thermal Fluid Sci. 13, 292–305.

Brücker, C., 1999. Structure and dynamics of the wake of bubbles and its relevance for bubble interaction. Phys. Fluids 11, 1781–1796.

Carpenter, G., Grossberg, S., 1987. ART-2: self-organization of stable category recognition codes for analog input patterns. Appl. Opt. 26, 4919–4930.

Clift, R., Grace, J.R., Weber, M.E., 1978. Bubbles, Drops and Particles. Academic Press, New York, NY.

Ellingsen, K., Risso, F., 1998. Measurements of the flow field induced by the motion of a single bubble. ICMF'98-286, Lyon, France, on CD.

Fan, L.S., Tsuchiya, K., 1990. Bubble Wake Dynamics in Liquids and Liquid-Solid Suspensions. Butterworths, Stoneham, MA.

Gonzalez, R.C., Wintz, P., 1987. Digital Image Processing. Addison-Wesley, Reading, MA.

Hardy, R.L., 1990. Theory and applications of the multiquadric–biharmonic method. 20 years of discovery. 1968–1988. Comput. Math. Appl. 19, 163–208.

Hassan, Y.A., Philip, O., 1997. A new artificial neural network tracking technique for particle image velocimetry. Exp. Fluids 23, 145–154.

Hassan, Y.A., Schmidl, W., Ortiz-Villafuerte, J., 1998. Investigation of three-dimensional two-phase flow structure in a bubbly pipe flow. Meas. Sci. Technol. 9, 309–326.

Hassan, Y.A., Ortiz-Villafuerte, J., Schmidl, W., 1999. Measurements of a rising single bubble in stagnant liquid. J. Flow Visualization & Image Processing 6, 129–137.

Hough, P.V.C., 1962. Method and means for recognizing complex patterns. US Patent No. 3069654.

Keane, R.D., Adrian, R.J., 1992. Theory of cross-correlation analysis of PIV images. App. Sci. Res. 49, 191–215.

Krishna, R., Urseanu, M.I., van Baten, J.M., Ellenberg, J., 1999. Wall effects on the rise of single gas bubbles in liquids. Int. Comm. Heat Mass Transfer 26, 781–790.

Lance, M., Bataille, J., 1991. Turbulence in the liquid phase of a uniform bubbly air–water flow. J. Fluid Mech. 222, 95–118.

Leavers, V.F., 1992. Shape Detection in Computer Vision Using the Hough Transform. Springer, London.

Leavers, V.F., 1993. Survey, which Hough transform?. CVGIP: Image Understanding 58, 250–264.

Lunde, K., Perkins, R.J., 1997. Observations of wakes behind spheroidal bubbles and particles. ASME FEDSM'97-3530, Vancouver, Canada, on CD.

Maneri, C.C., Mendelson, H.D., 1968. The rise velocity of bubbles in tubes and rectangular channels as predicted by wave theory. AIChE J. 14, 295–300.

Maas, H.G., Gruen, A., Papantoniou, D., 1993. Particle tracking velocimetry in three-dimensional flows. Part I. Photogrammetric determination of particle coordinates. Exp. Fluids 15, 133–146.

O'Hern, T.J., Torczynski, J.R., Shagam, R.N., Blanchat, T.K., Chu, T.Y., Tassin-Leger, A.L., Henderson, J.A., 1997. Optical diagnostics for turbulent and multiphase flows: particle image velocimetry and photorefractive optics. SANDIA Report SAND94-2589. Albuquerque, NM.

Okamoto, K., Schmidl, W., Hassan, Y., 1995. New tracking algorithm for particle image velocimetry. Exp. Fluids 19, 342–347.

Ortiz-Villafuerte, J., 1999. Three-dimensional experimental investigation of the shape and dynamics of a rising bubble in stagnant water with particle tracking velocimetry. Ph.D. Dissertation, Texas A&M University, College Station, TX.

Saffman, P.G., 1956. On the rise of small air bubbles in water. J. Fluid Mech. 1, 249–274.

Schmidl, W.D., 1999. Three-dimensional experimental investigation of the two-phase flow structure in a bubbly pipe flow. Ph.D. Dissertation, Texas A&M University, College Station, TX.

Tasuge, H., Hibino, S., 1975. Effect of column wall on the ascending velocity of gas bubbles in various liquids. Int. Chem. Eng. 15, 186–192.

Uno, S., Kintner, R.C., 1956. Effect of wall proximity on the rate of rise of single air bubbles in a quiescent liquid. AIChE J. 2, 420–425.